Outline

1. Properties of silicate liquids
2. Adiabatic decompression melting
   - Melting temperature(s) of lherzolite
   - Model for mid-ocean ridges
3. *Melting in mantle plumes*
4. *Effects of water and pyroxenite/eclogite veins*
5. *Phase equilibria of melting (only the basics)*
6. *Melt percolation models..... U series isotopes*

Some questions about plumes in general and the Hawaiian plume in particular

1. How big is the plume in horizontal dimensions?
   - Width of temperature anomaly
   - Width of upwelling velocity anomaly
   - Width of melting region
   - Width(s) of isotopic anomalies
   - Widths at depth >200km versus width in the melting region (90 - 150km)
2. How hot is the plume (and why do we think so)
   - At its core
   - At the fringes of the melting region

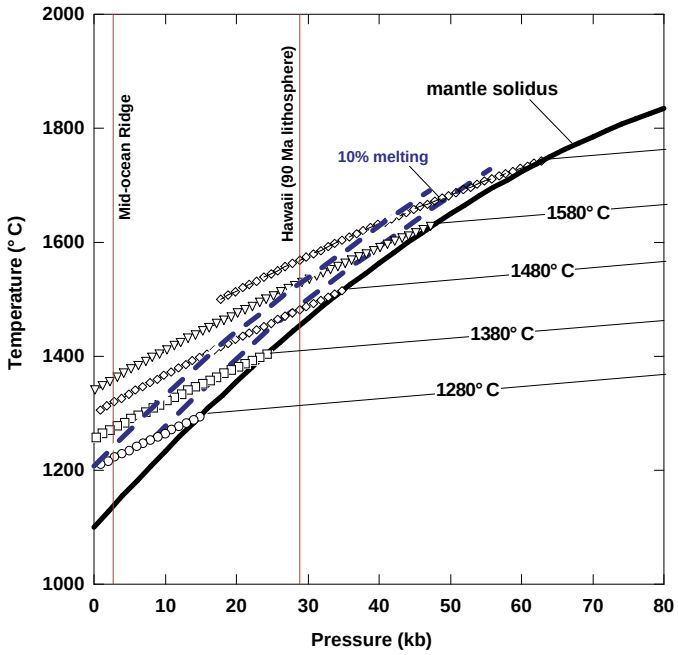

There is currently one available model for the Hawaiian plume

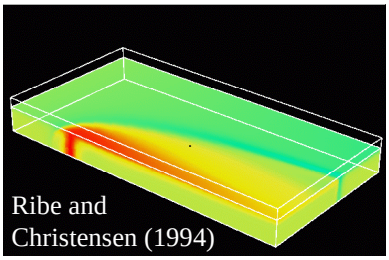

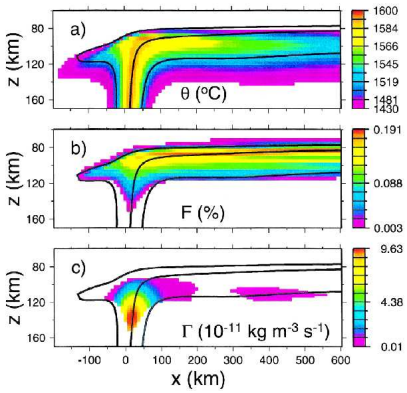

Melt Supply to Crust-- Hawaiian Plume

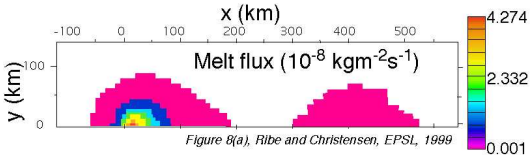

Figure 8(a), Ribe and Christensen, EPSL, 1999

R&C (1999) θ at 110km depth

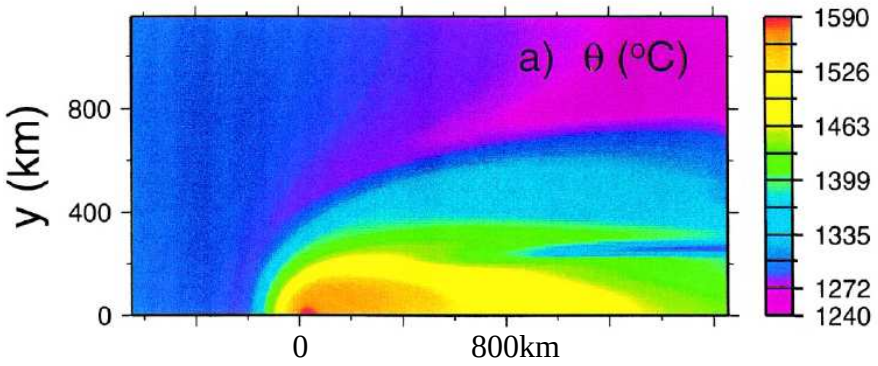

QuickTime™ and a TIFF (LZW) decompressor are needed to see this picture.

-200 0 200 400km

R&C (1999) generate the plume with a radial thermal anomaly at the bottom of the box (400km depth). At 170 km depth T is approx.:

$$\Delta\theta(r) = \Delta\theta_o \exp\left(-\frac{r^2}{a_\theta^2}\right)$$

Where a_θ 65 km, and θ_o = 300K. These values depend in detail on the viscosity structure of the plume. The width of the thermal anomaly is about 130km (1σ at170km), which is the full width at about 17% of θ_{max}. Constraints are (a) buoyancy flux, (b) H/W of swell, (c) rate of magma production

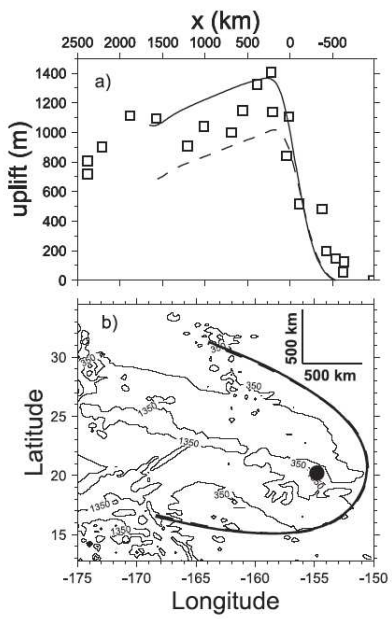

Fig. 2. (a) Squares: estimates of uplift along the axis of the Hawaiian swell [4,24]. Solid and dashed lines: uplift predicted by the reference model with and without depletion buoyancy,

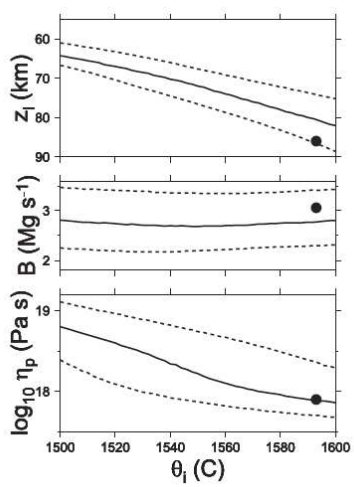

Fig. 3. Solid lines: values of lithospheric thickness z_l (top panel), thermal buoyancy flux B (middle), and plume viscosity η_p (bottom) required to predict simultaneously a total melting rate $M = 1.4 \times 10^4$ kg s^{-1}, maximum uplift $H = 1350$ m, and swell width $W = 600$ km, as functions of potential temperature θ_i of incipient melting. Dashed lines: maximum allowable ranges of z_l, B, and η_p consistent with estimated uncertainties in M (± 1600 kg s^{-1}), H (± 100 m), and W (± 50 km). Dots: values of θ_i, z_l, B, and η_p for the reference model.

QuickTime™ and a TIFF (LZW) decompressor are needed to see this picture.

Integrated amount of melting

Melting rate

In the R&C (1999) model, the maximum degree of melting reached is about 20%. The core of the plume does not melt above 90km depth. At the edges of the melting region, melting stops at about 120km depth. At 120 km depth the plume width has increased by about 1.6 times as result of spreading beneath the lithosphere

In the R&C (1999) model, the width of the melting region at 120km depth is about 120 km, and the total melt production varies horizontally as:

$$G(r) \approx G_o \exp\left(-\frac{r^2}{a_G^2}\right)$$

where G_o is about 0.05 $m^3/m^2/yr$, and a_G 30 km. The width of the melting region is about 1/3 the radius of the thermal anomaly (which has spread to 100km width at 120 km depth).

R&C (1999) do not specifically mention the upwelling velocities in their model plume. From the melting rate at the core of the plume it can be inferred that the maximum upwelling rate is about 35 cm/yr. This value is similar to that obtained by Watson and McKenzie (1991) with a simpler axisymmetric model.

Upwelling rate, plume width and temperature are all interrelated. The relationships, and the effects of the assumptions about mantle rheology, were investigated by Hauri et al. (1994)

Arrangement *a la* DePaolo et al. 2001

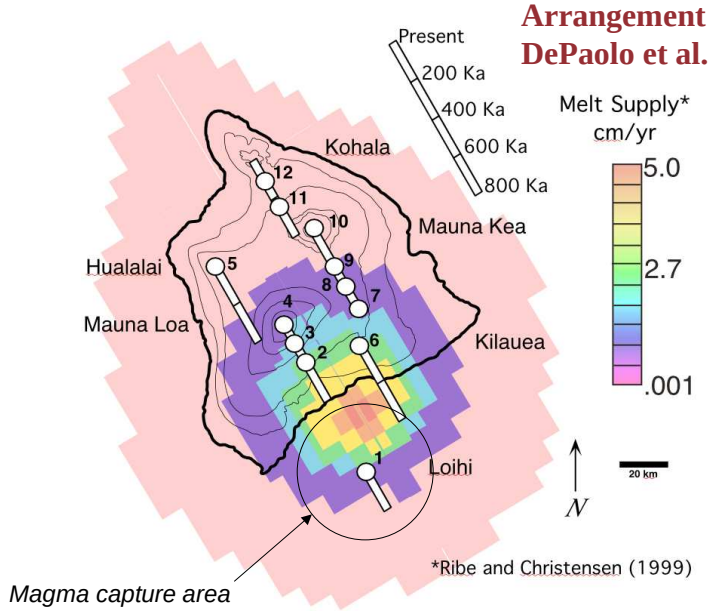

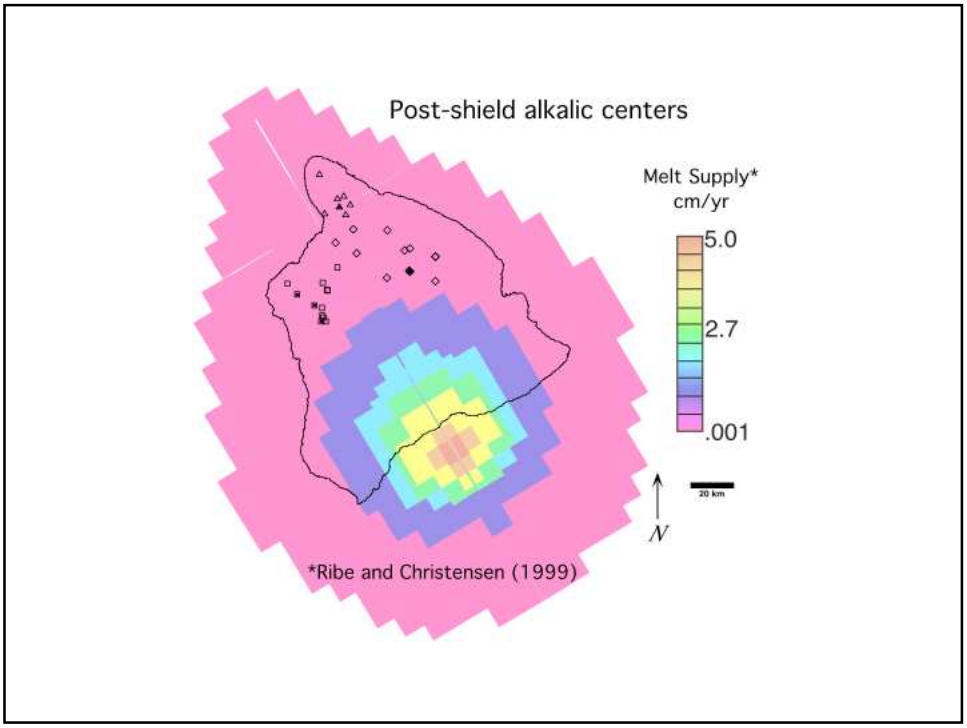
Post-shield alkalic centers
Melt Supply*
cm/yr
5.0
2.7
.001
20 km
N
*Ribe and Christensen (1999)

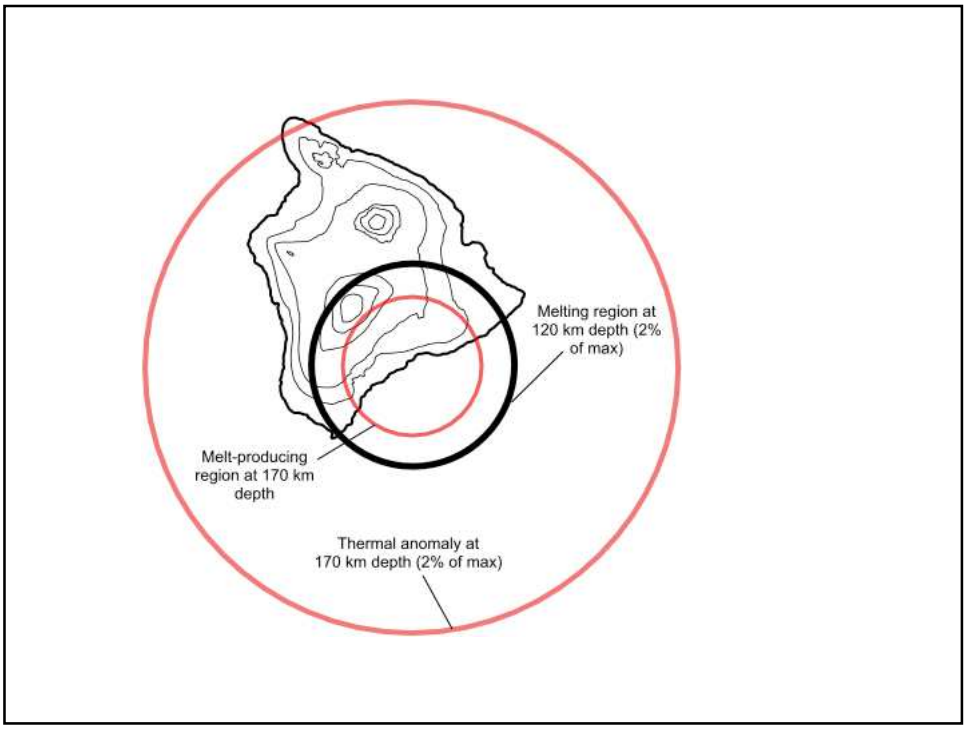
Melting region at
120 km depth (2%
of max)
Melt-producing
region at 170 km
depth
Thermal anomaly at
170 km depth (2% of max)

G. Hart and DePaolo (in prep), solidus from Hirschmann (2000). Equations from Asimow et al

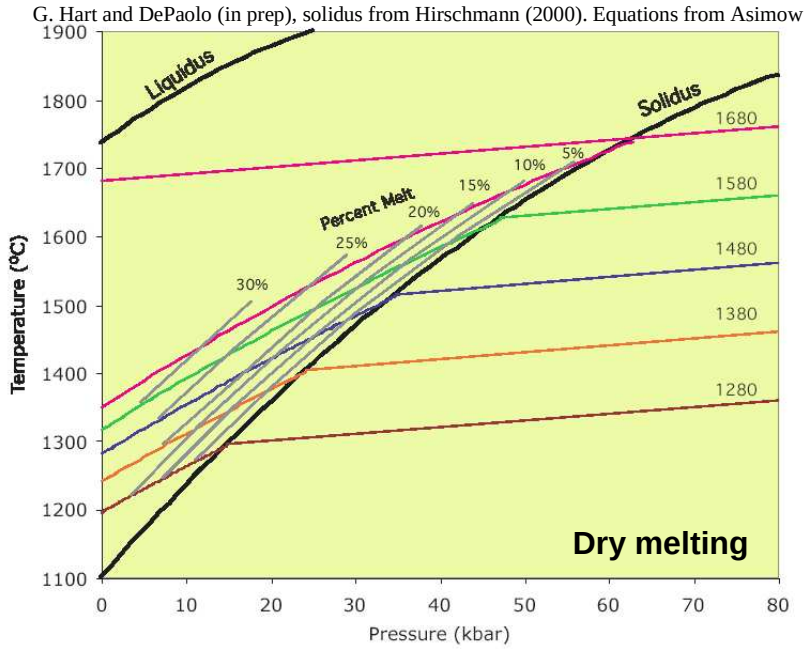

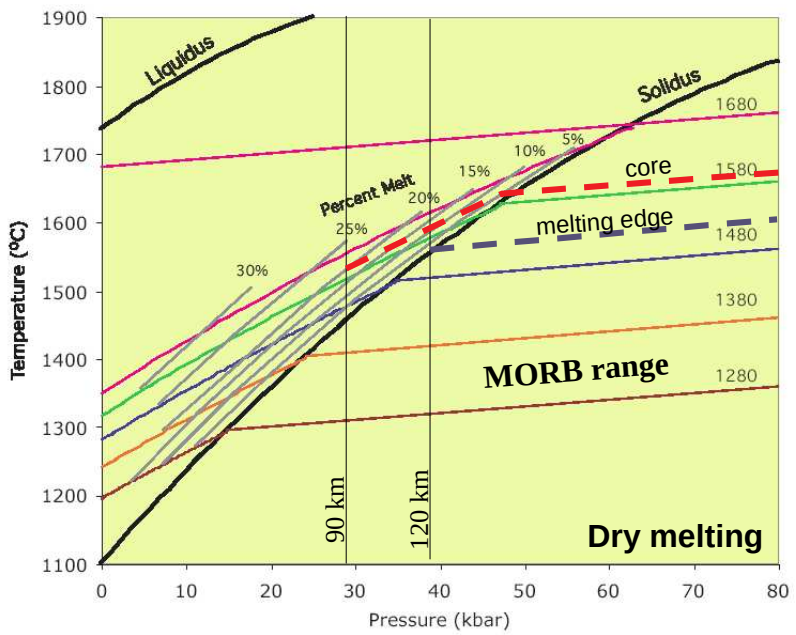

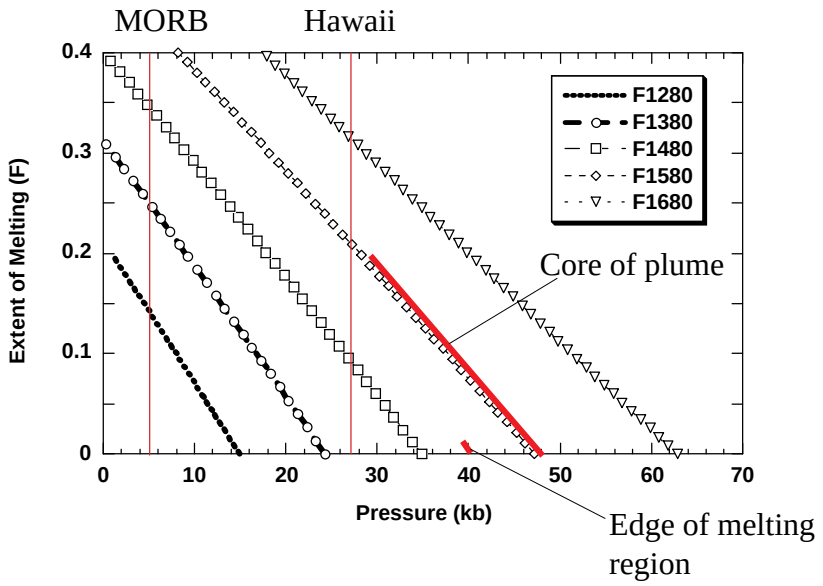

Effect of H_2O on melting temperature, from Hirschmann et al. (2001)

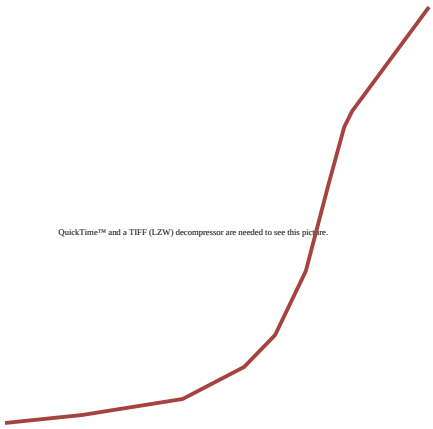

Effect of H_2O on melting temperature, from Hirschmann et al. (2001)

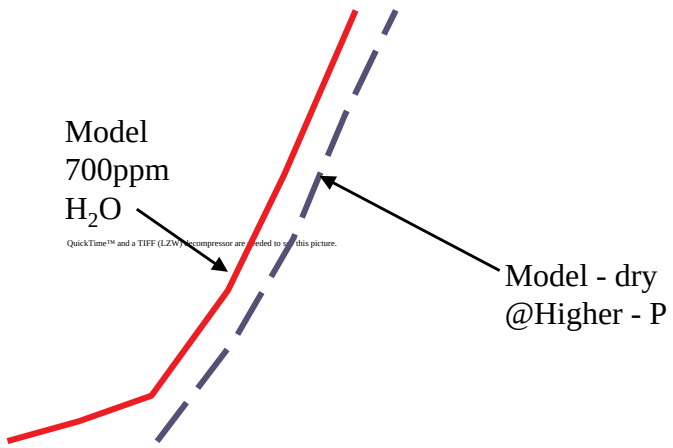

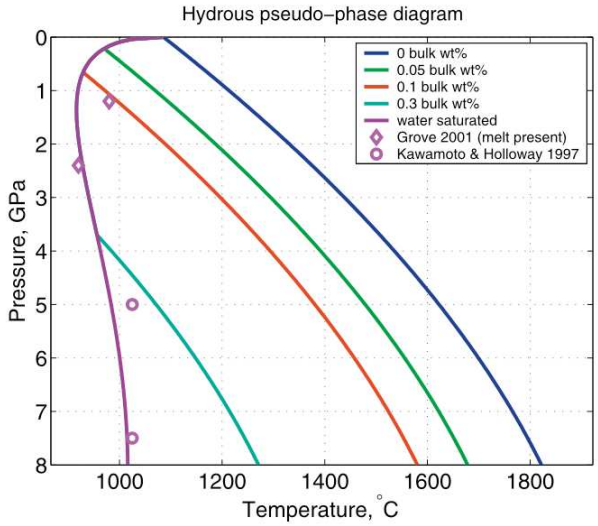

Figure 3. The solidus for different bulk water contents of the system. Solidus depression is linear with dissolved water. It is bounded by the saturation of water in the melt, a function of pressure.

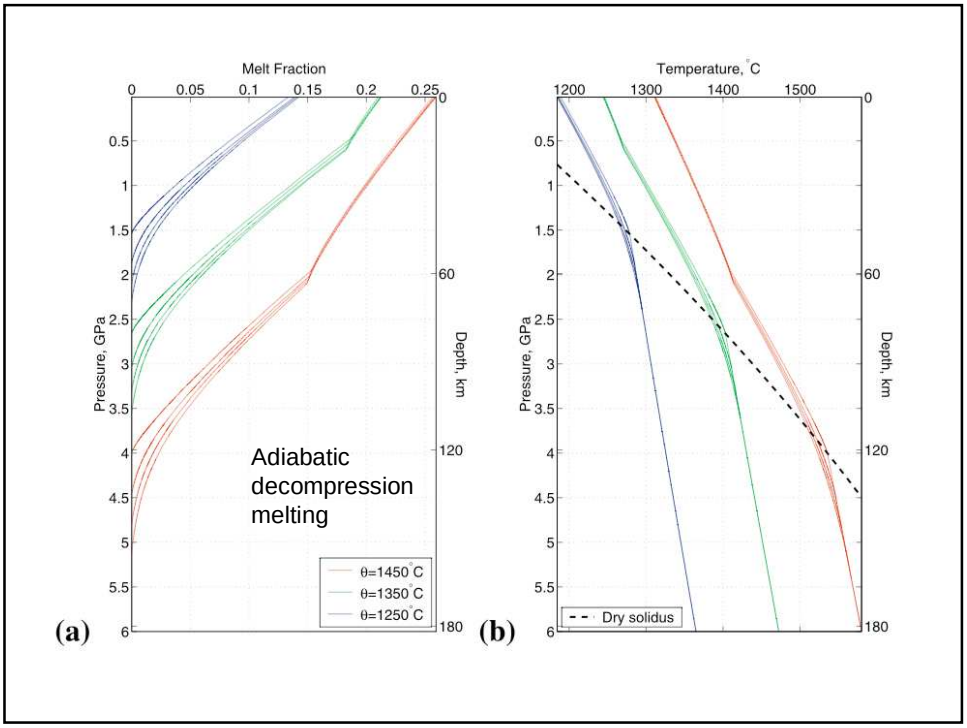
Melt Fraction
Pressure, GPa
Depth, km
Adiabatic decompression melting
θ=1450°C
θ=1350°C
θ=1250°C
(a)
Temperature, °C
Dry solidus
(b)

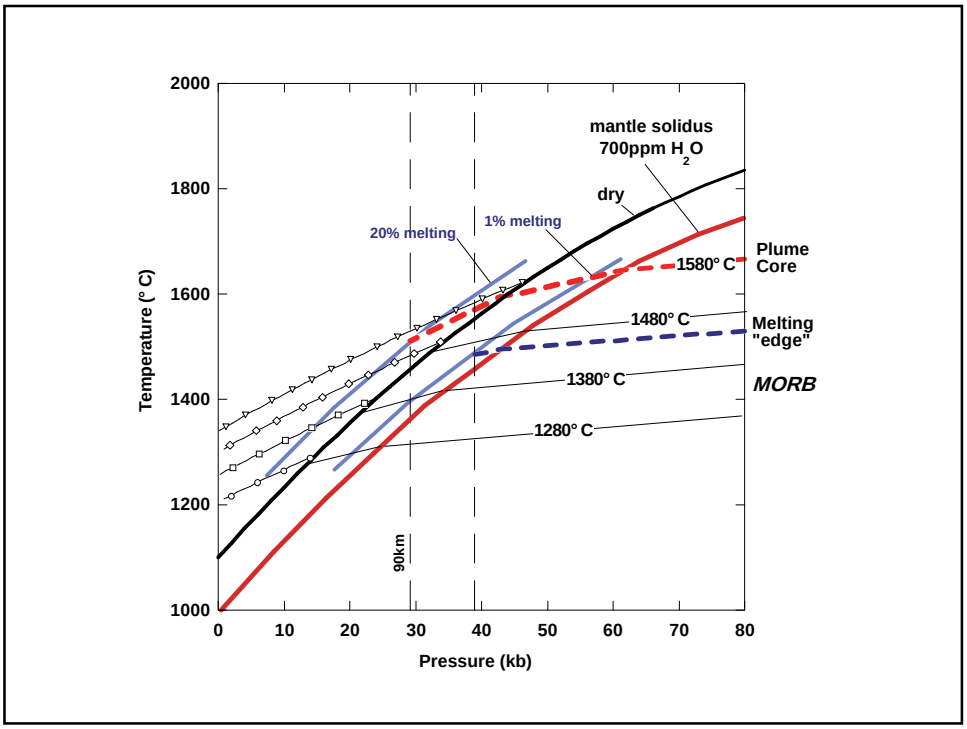
mantle solidus
700ppm H2O
dry
20% melting
1% melting
1580° C
Plume Core
1480° C
Melting "edge"
1380° C
MORB
1280° C
90km
Temperature (° C)
Pressure (kb)

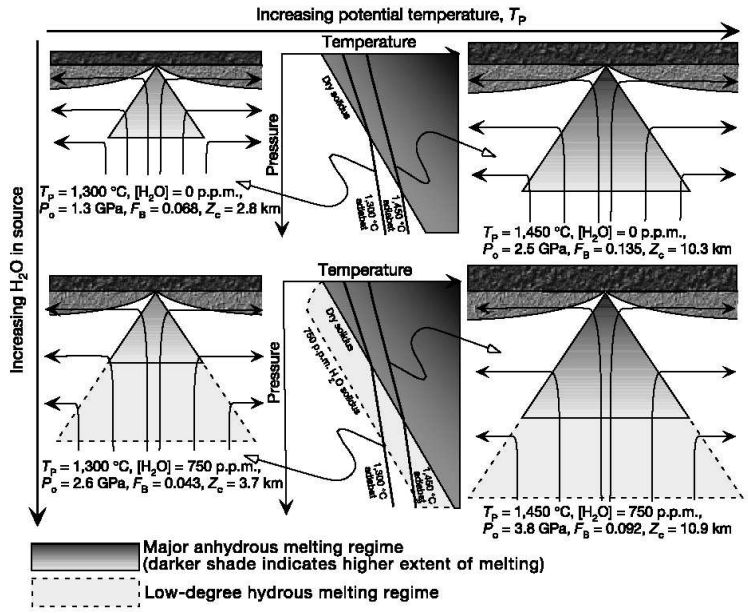

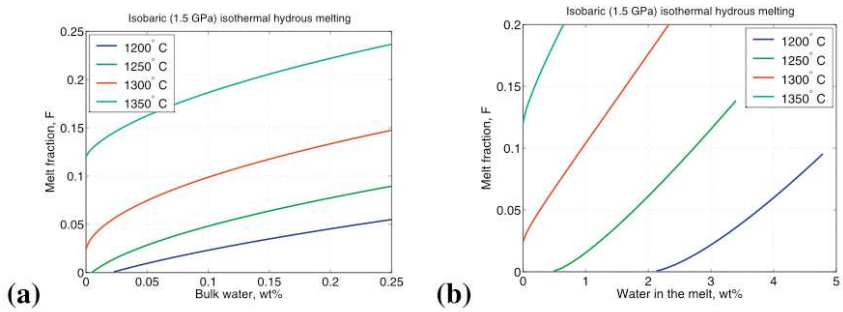

Figure 5. Degree of melting as a function of the water in the system, holding the temperature (see figure) and pressure (1.5 GPa) constant. Modal cpx is 17% in the unmelted solid. (a) F as a function of $X^{bulk}_{H_2O}$. Compare to *Gaetani and Grove* [1998, Figure 13a]. (b) F as a function of water dissolved in the melt. Bulk distribution coefficient of water is assumed to be 0.01.

Magma generation and composition summary

- Two main types of basalt
  - Tholeiitic
  - Alkaline
- **Tholeiitic basalt** forms at lower pressure and with higher melt fractions
- **Alkali basalt** forms only at higher pressure and with small melt fractions
- **Andesite** forms in island arcs at high pressure because of the abundacne of H_2O

(P.S. The following is qualitative, but at least it may be understandable)

The difference between Tholeiitic and Alkali basalt can be understood with this diagram.

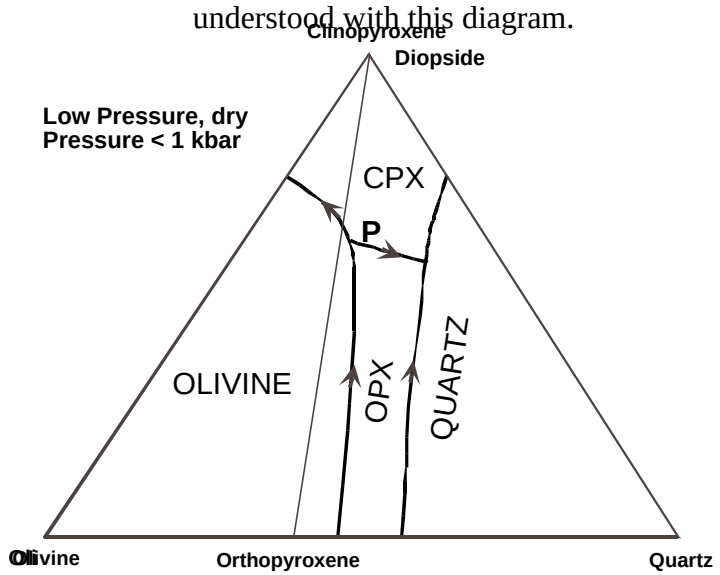

Tholeiitic basalt will crystallize OPX and with extensive fractional crystallization can eventually crystallize quartz

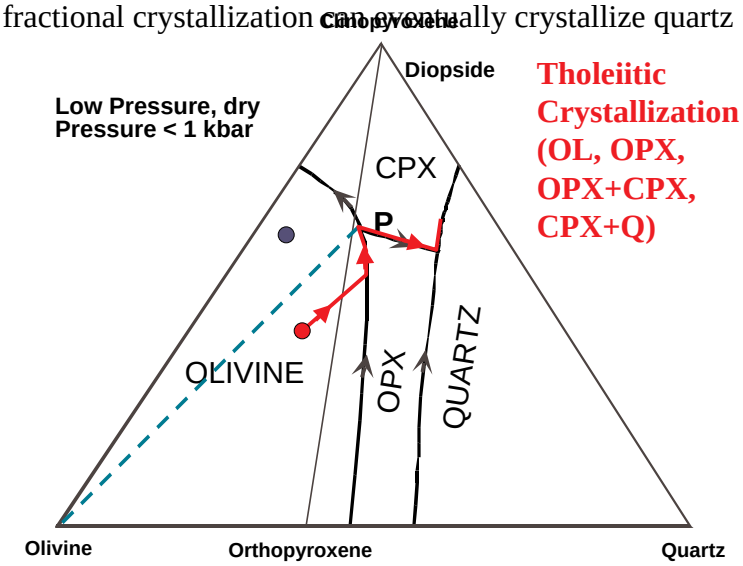

Alkali basalt will not crystallize OPX or Quartz

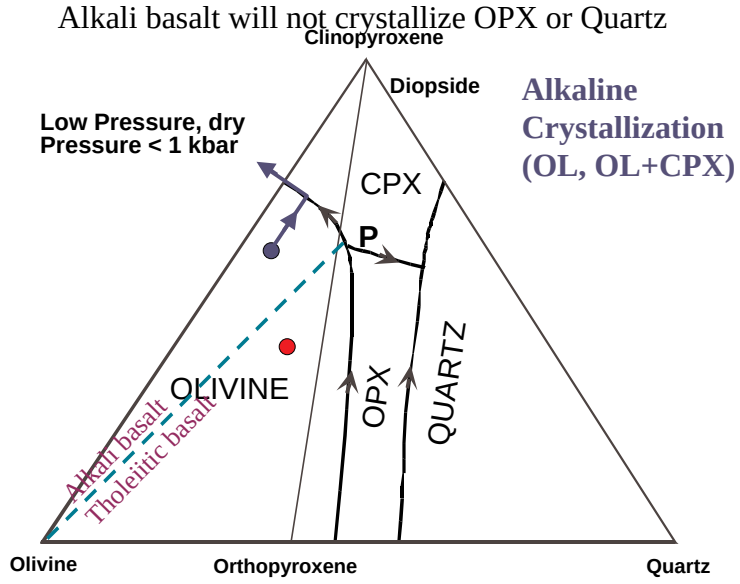

The high pressure version of the phase diagram shows why Alkali basalt is formed at high pressure

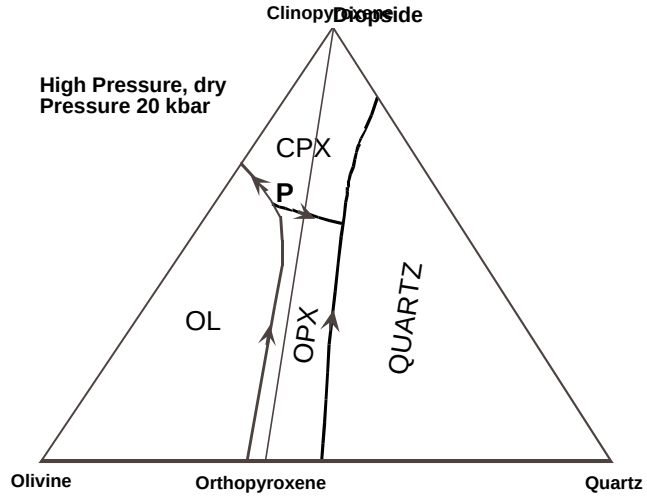

Mantle peridotite is OL-rich. This version of the diagram shows approximate SiO_2 contents of rocks

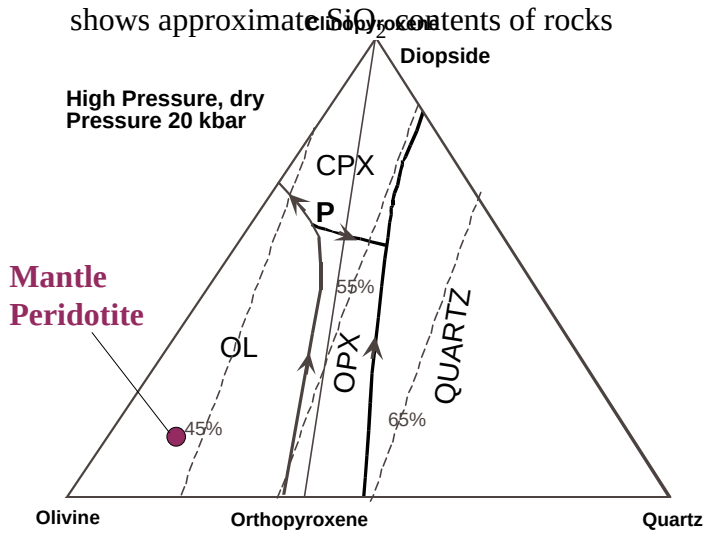

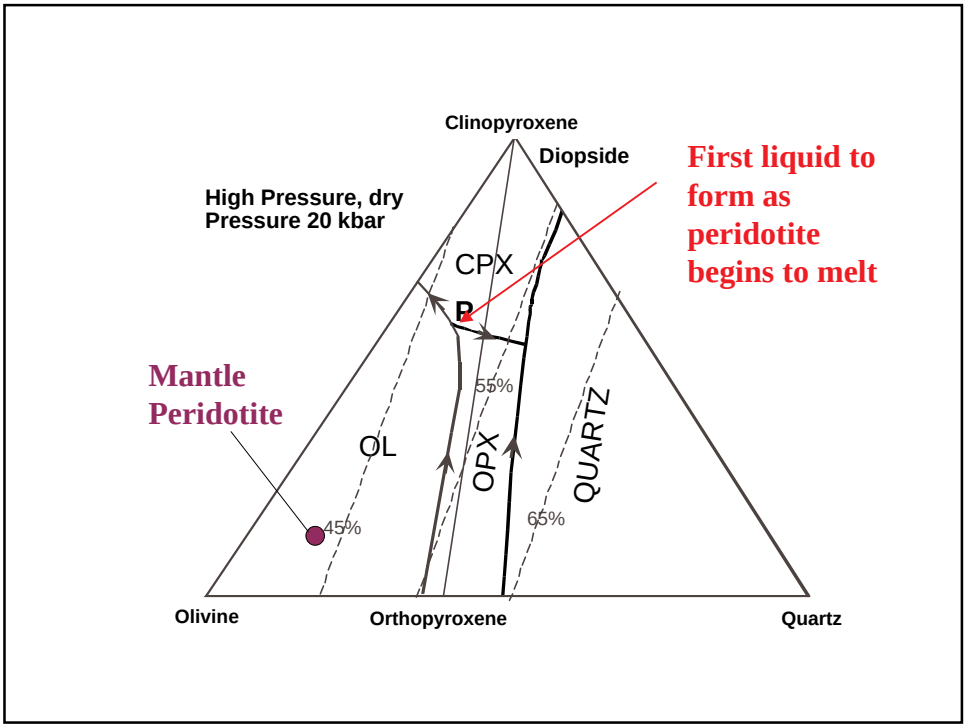
Clinopyroxene
Diopside
High Pressure, dry
Pressure 20 kbar
First liquid to form as peridotite begins to melt
CPX
P
Mantle Peridotite
55%
OL
OPX
QUARTZ
45%
65%
Olivine
Orthopyroxene
Quartz

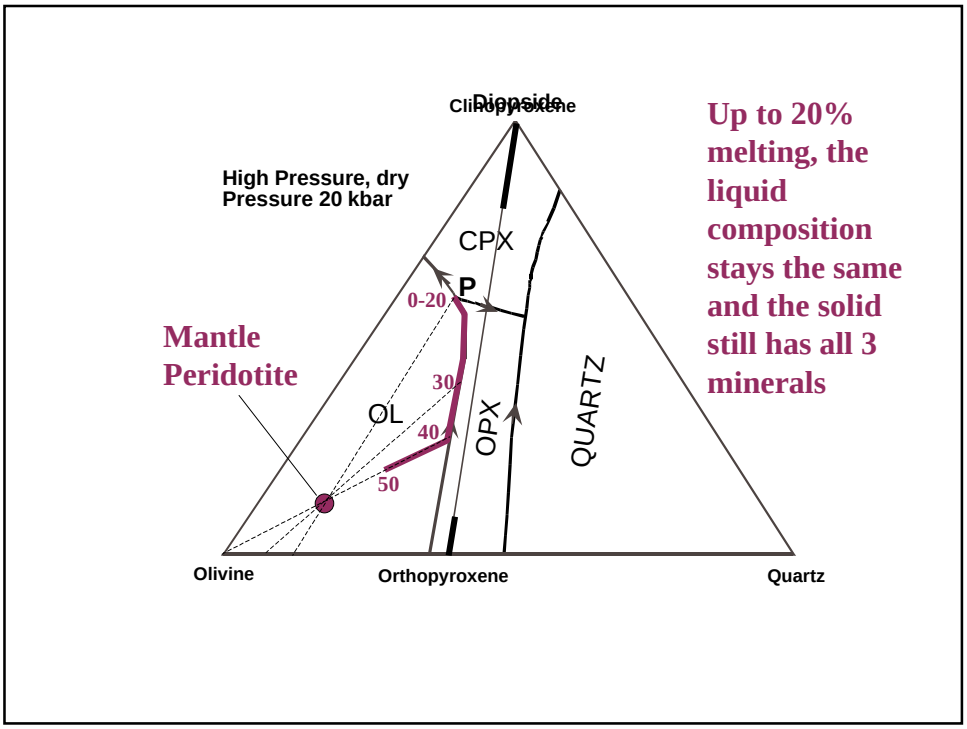
Clinopyroxene
Diopside
High Pressure, dry
Pressure 20 kbar
Up to 20% melting, the liquid composition stays the same and the solid still has all 3 minerals
CPX
P
0-20
Mantle Peridotite
30
OL
40
OPX
QUARTZ
50
Olivine
Orthopyroxene
Quartz

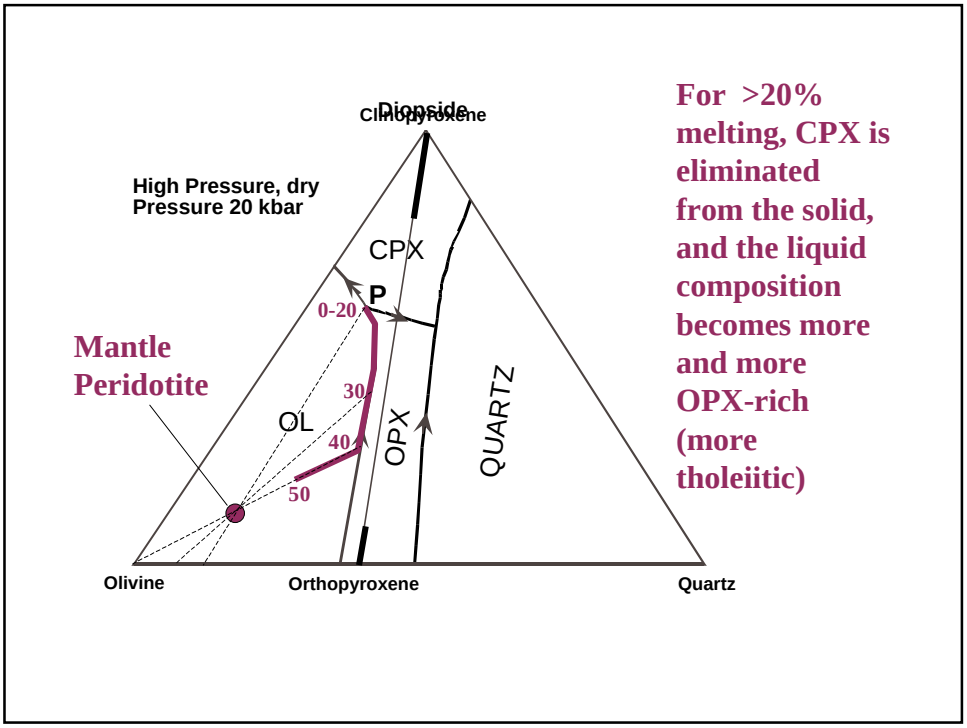
Diopside
Clinopyroxene
High Pressure, dry
Pressure 20 kbar
CPX
P
0-20
Mantle
Peridotite
30
OL
40
OPX
QUARTZ
50
Olivine
Orthopyroxene
Quartz
For >20% melting, CPX is eliminated from the solid, and the liquid composition becomes more and more OPX-rich (more tholeiitic)

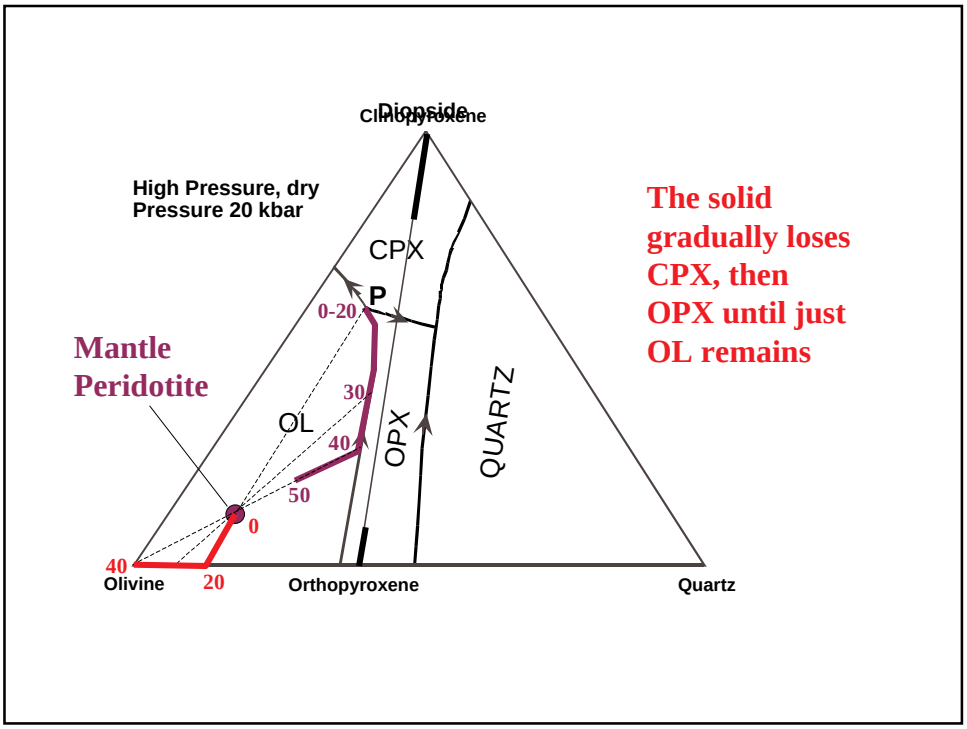
Diopside
Clinopyroxene
High Pressure, dry
Pressure 20 kbar
CPX
P
0-20
Mantle
Peridotite
30
OL
40
OPX
QUARTZ
50
0
40
Olivine
20
Orthopyroxene
Quartz
The solid gradually loses CPX, then OPX until just OL remains

When liquids formed at P>20kb are brought to the surface and crystallize, those corresponding to lower % melts are seen to be alkali basalt, those at higher % melts are tholeiitic

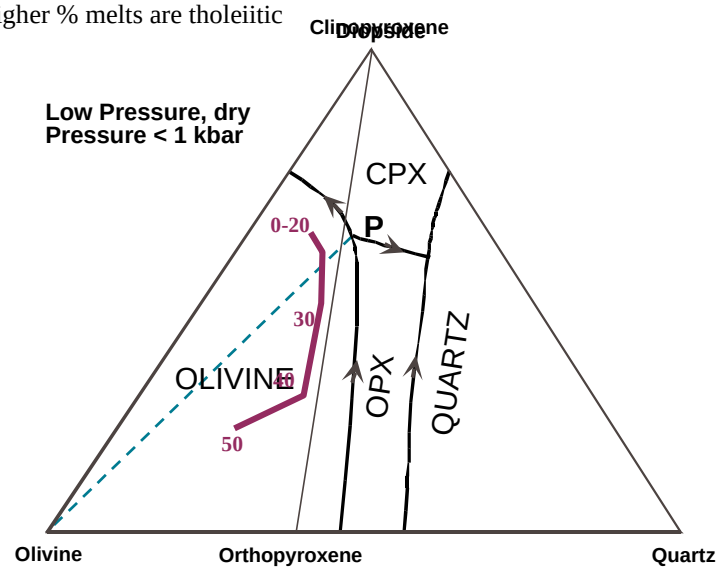

Summary diagram

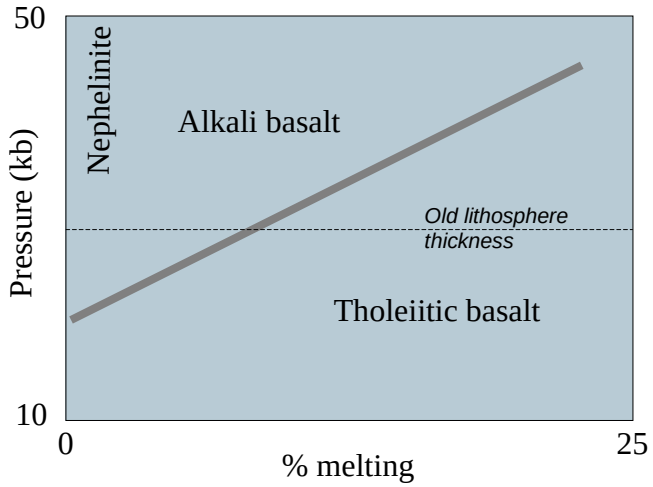

Examples - Hawaii has high melt fractions at high pressure and hence the most common lavas are tholeiitic. Tahiti is mostly alkaline (it is a weaker plume). MORB are always tholeiitic

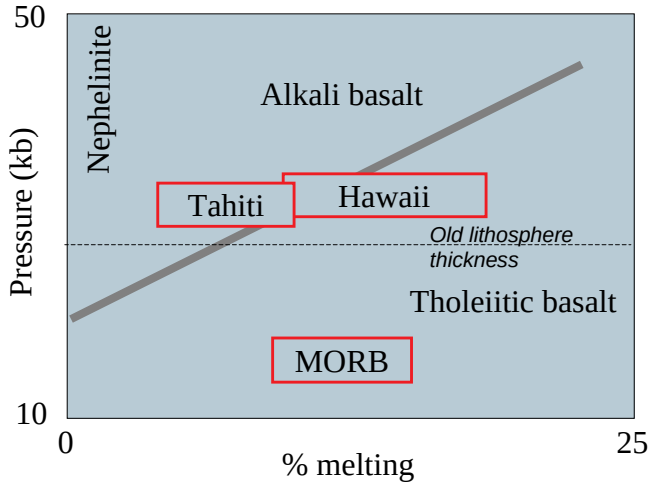

QuickTime™ and a
TIFF (LZW) decompressor
are needed to see this picture.

Backscattered electron image of an experiment "charge" showing vitreous carbon spheres. During the experiment the peridotite melts and the liquid is squeezed into to the space between the spheres (P = 1.5 Gpa)

QuickTime™ and a
TIFF (LZW) decompressor
are needed to see this picture.

QuickTime™ and a
TIFF (LZW) decompressor
are needed to see this picture.

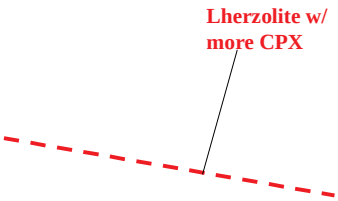

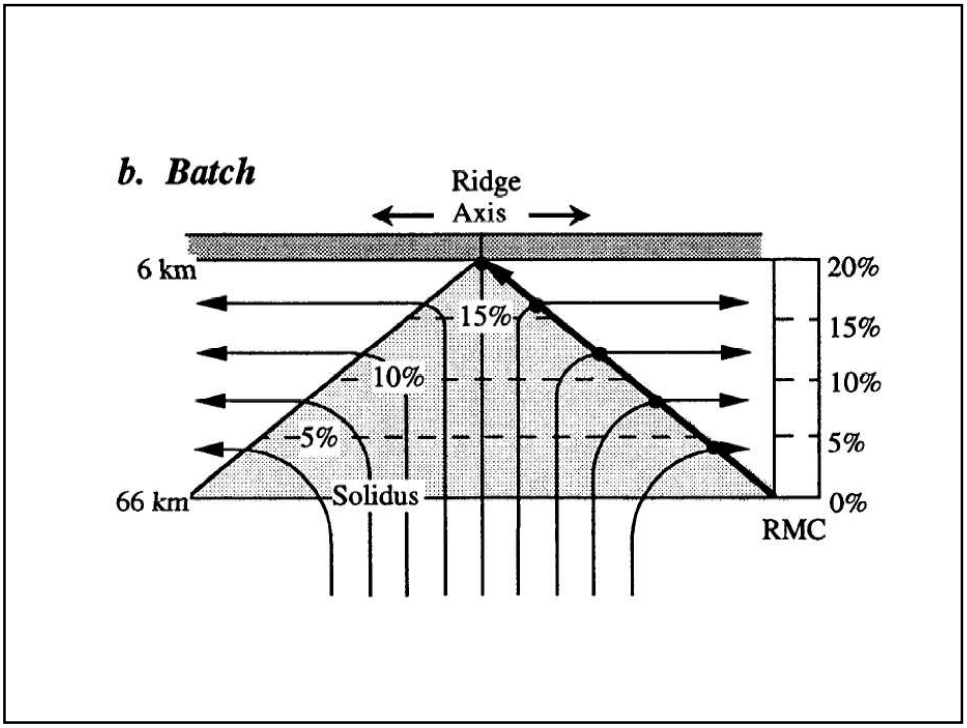
b. Batch
Ridge
Axis
6 km
66 km
15%
10%
5%
Solidus
20%
15%
10%
5%
0%
RMC

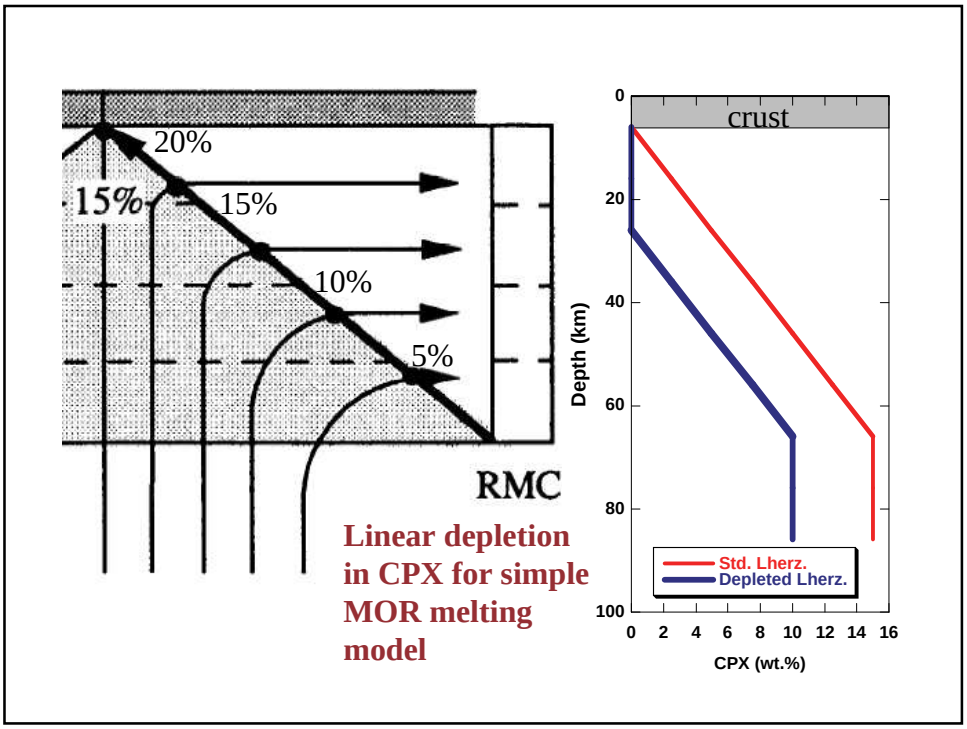
20%
15%
15%
10%
5%
RMC
Linear depletion in CPX for simple MOR melting model
crust
Depth (km)
CPX (wt.%)
Std. Lherz.
Depleted Lherz.
0
20
40
60
80
100
0 2 4 6 8 10 12 14 16

Lherzolite: Peridotite with Olivine > Opx + Cpx

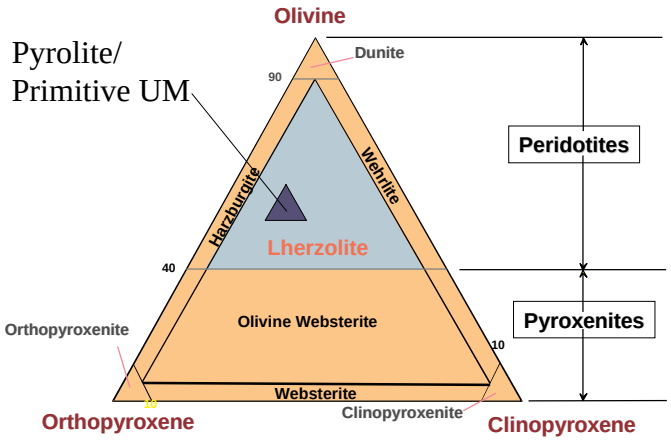

In plumes, depletion isopleths correspond to CPX* mode

0%

CPX*

8%

QuickTime™ and a TIFF (LZW) decompressor are needed to see this picture.

15%

*(*Need to include garnet in the model here.)*

For trace element partitioning we use the expression:

$$\frac{C_{liq}}{C_0} = \frac{1}{D_i + F(1 - D_i)}$$

But, what is F for real situations?

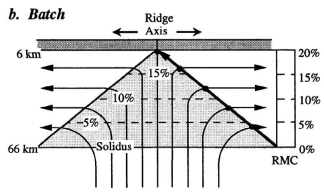

QuickTime™ and a TIFF (LZW) decompressor are needed to see this picture.

For MOR model mean F is about 0.05 to 0.10. Varies from 0.20 to 0.00x over the melt zone.

For Hawaii model mean F is about 0.04 to 0.05; averaged over entire melting region. Varies from 0.2 to 0.00x.

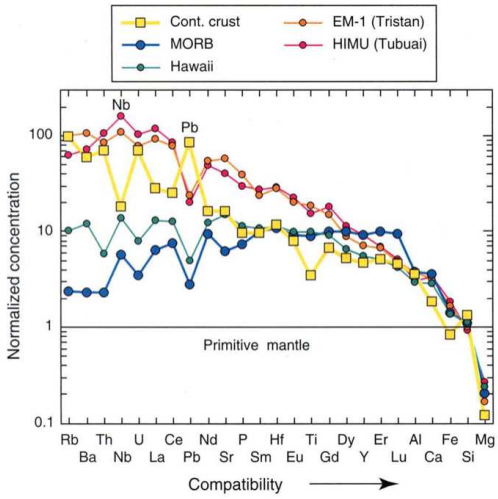

$$\frac{C_{liq}}{C_0} = \frac{1}{D_i + F(1 - D_i)}$$

$$\frac{C_{liq}}{C_0} = \frac{1}{F}$$ *For D_i=0*

For weaker plumes, mean F may be 0.01; but also lavas may represent small F as volcano drifts off of the plume.

Other experiments showing difference between tholeiitic and alkalic basalt

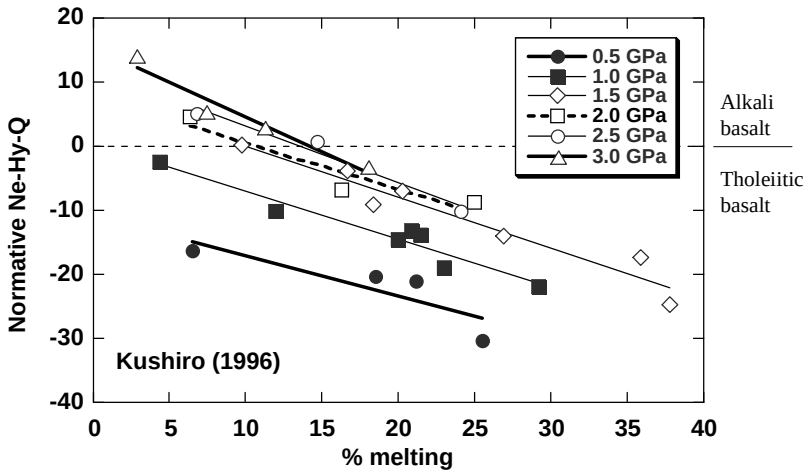

QuickTime™ and a
TIFF (LZW) decompressor
are needed to see this picture.

Veins of eclogite/pyroxenite in the mantle: melting effects

one of the difficulties in making generalizations about the behavior of pyroxenites in the mantle is their extraordinary compositional range

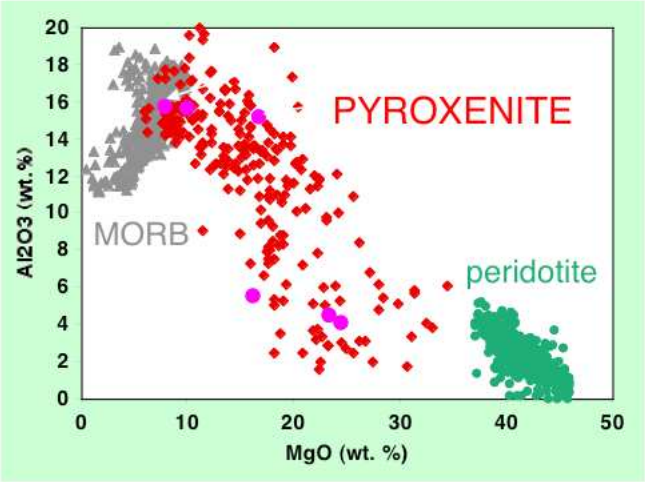

Could we detect a contribution of pyroxenites/eclogites from a compositional signature in mantle-derived magmas?

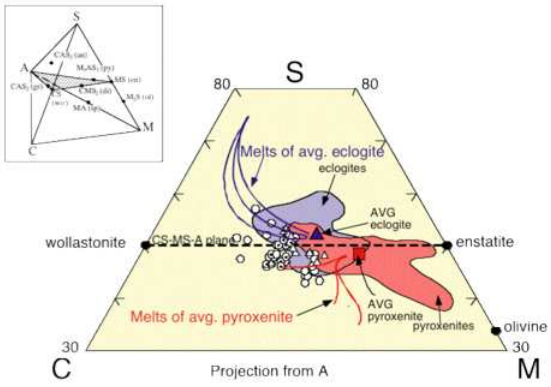

Despite their compositional diversity, the solidi of pyroxene-rich mantle rocks are *generally* (but not always) lower than those of peridotites.

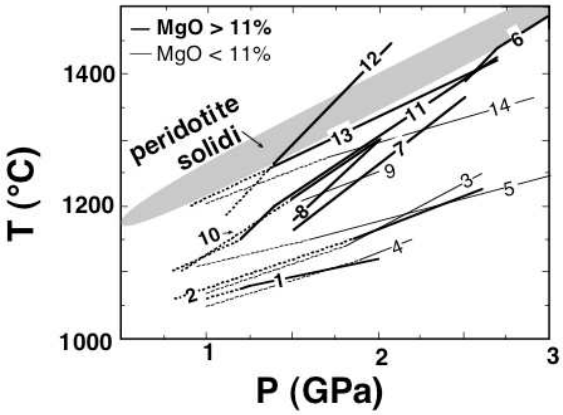

this leads to the important concept that the pyroxene-rich lithologies will begin to melt separately and at greater depth than peridotites during decompression melting

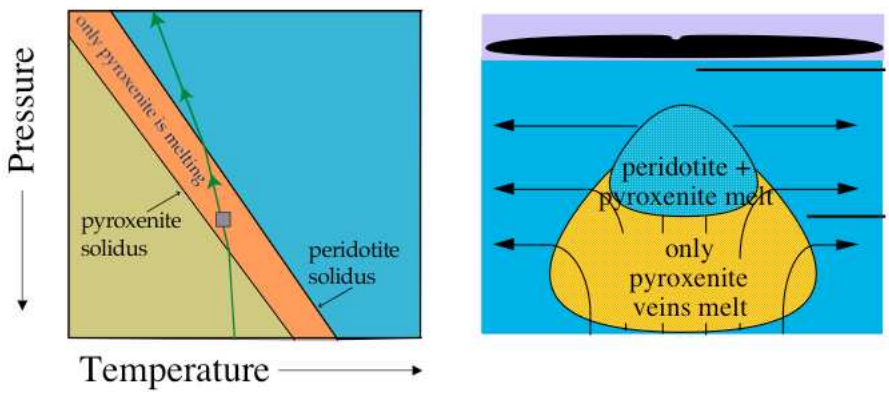

how will the difference in solidi between pyroxene-rich rocks and peridotites influence adiabatic melting?

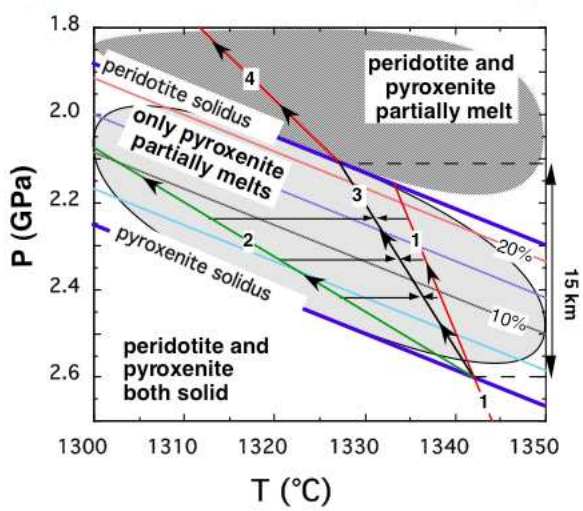

⇒ pyroxenite melting is enhanced by the thermal buffering of the peridotite, but the peridotite reaches its solidus at a lower P and T

we can do a full thermodynamic model of melting of a mixed peridotite + pyroxenite source using MELTS

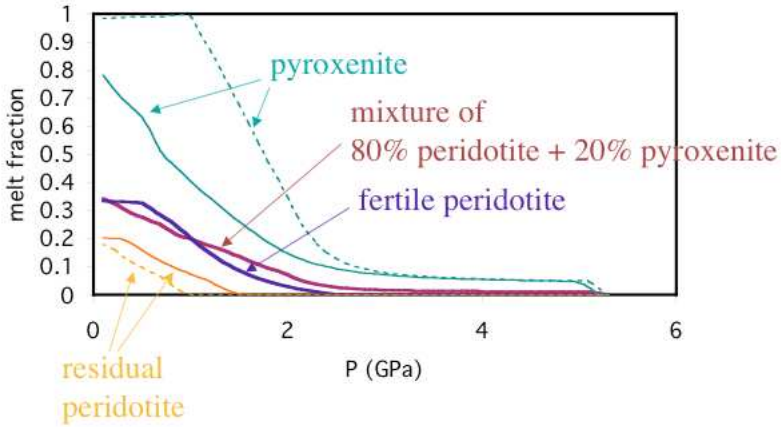

this demonstrates that although the pyroxenite melts to high degrees when embedded in residual peridotite, the total amount of melting of the source is *not* enhanced

Model for melt percolation; 1D steady state upwelling

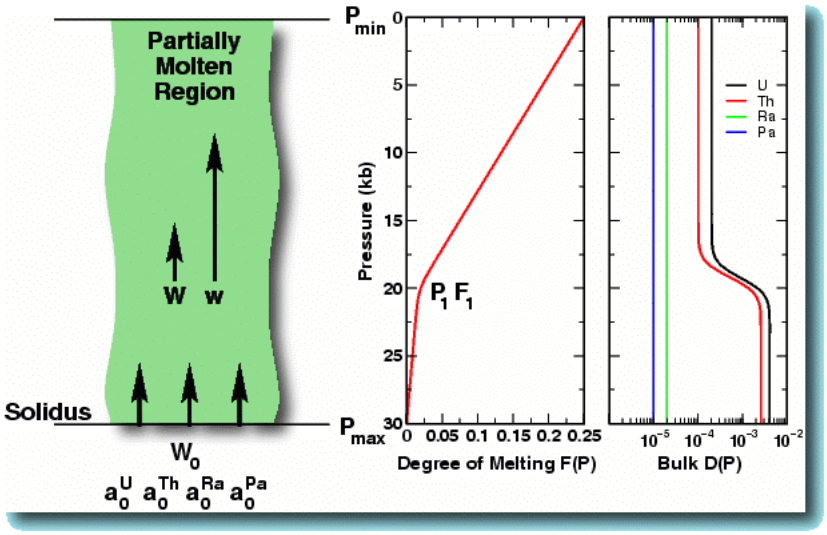

melting column, the flux of melt and solid as a function of height, z, in the column can be written:

$$\rho_f \phi w = \Gamma_0 z \quad (2)$$

$$\rho_s(1-\phi)W = \rho_s W_0 - \Gamma_0 z \quad (3)$$

where w is the one-dimensional melt velocity and W is the solid velocity [see also 18]. The term

$$\Gamma_0 = \frac{\rho_s W_0 F_{max}}{d} \quad (4)$$

is the constant melting rate in the column. Equation (4) approximates melting by adiabatic decompression by setting the melting rate proportional to the mantle upwelling rate, W_0. F_{max} is the maximum degree of melting attained at the top of the column (i.e., at height $z = d$). Here the melting rate is constant, but these equations can be readily extended to include variable melting rates (see Appendix A).

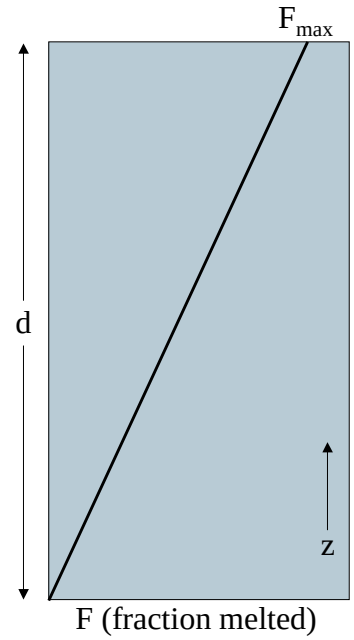

To determine $\phi(z)$ requires an additional functional relationship between porosity and melt and solid velocities. Here we use a simplified form of Darcy's law

$$\phi(w - W) = \frac{k_0}{\mu}\phi^n(1-\phi)\Delta\rho g \quad (6)$$

to govern the separation of melt from solid. k_0 controls the permeability and depends upon the

$$v_{melt} \propto \frac{(\rho_{solid} - \rho_{liq})\phi^2}{\mu_{liq}}$$

Equations (2) and (3) show that the melt and solid fluxes simply balance melt production and vary linearly with height in the column. In particular, eq. (2) shows that the melt flux increases with z but at any height, the product of porosity and melt velocity is fixed. If we note that $F = F_{max} z/d$ is the degree of melting at height z, then eqs. (2) and (4) can be combined to show that the relationship between melt velocity and porosity in steady state is:

$$w = W_0 \frac{\rho_s F}{\rho_f \phi} \qquad (5)$$

If the melt does not separate from the solid ($w \to W_0$) then the porosity will be comparable to the degree of melting ($\phi \sim F$). Very efficient melt extraction ($w \gg W_0$) implies that the residual porosity must be very small and $\phi \ll F$. Once $F(z)/\phi(z)$ is known at any height, the melt velocity is determined.

For F/ϕ =10, w/W_0 12

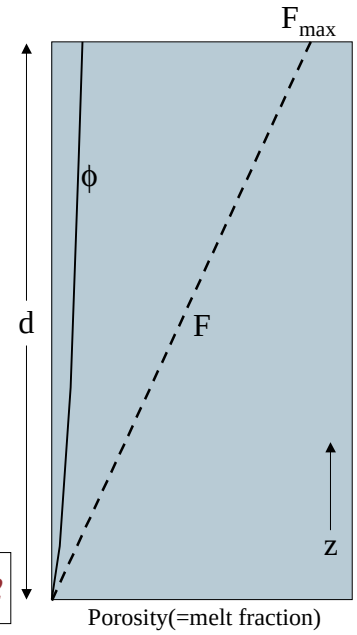

We begin with the general equation governing conservation of mass for each parent–daughter pair in a decay series of radioactive elements

$$\frac{\partial}{\partial t}\left[\rho_f \phi + \rho_s(1-\phi) D_i\right] c_i^f + \nabla \cdot \left[\rho_f \phi v + \rho_s (1-\phi) D_i V\right] c_i^f = \lambda_{i-1}\left[\rho_f \phi + \rho_s(1-\phi) D_{i-1}\right] c_{i-1}^f - \lambda_i \left[\rho_f \phi + \rho_s (1-\phi) D_i\right] c_i^f \qquad (1)$$

Here ρ_f and ρ_s are the densities of the melt and solid, respectively, ϕ is the volume fraction of melt (porosity), v is the melt velocity and V is the solid velocity. For each element $i = 1,2,3\ldots$ in the decay series, D_i is its bulk partition coefficient, c_i^f is its concentration in the melt and λ_i is its decay constant. Additional parameters and notation are given in Table 1. The first nuclide in the decay chain, ^{238}U, has no parent and therefore $\lambda_0 = 0$. For simplicity, eq. (1) disregards dif-

the daughter element. The radiogenic production term depends primarily on the "effective velocity" of each element i [e.g., 10,11]

$$w_{\mathrm{eff}}^{i} = \frac{\rho_{\mathrm{f}}\phi w + \rho_{\mathrm{s}}(1-\phi)D_i W}{\rho_{\mathrm{f}}\phi + \rho_{\mathrm{s}}(1-\phi)D_i}$$

$$= W_0 \frac{D_i + (1-D_{\mathrm{i}})F_{\max}\zeta}{D_i + (\rho_{\mathrm{f}}/\rho_{\mathrm{s}} - D_i)\phi}$$

$$\approx W + \frac{1}{1+D_i/\phi}(w-W) \qquad (12)$$

which is a weighted combination of the melt and solid velocities. Elements with partition coefficients greater than the porosity ($D_i \gg \phi$) travel near the solid velocity. Very incompatible elements ($D_i \ll \phi$) travel near the melt velocity.

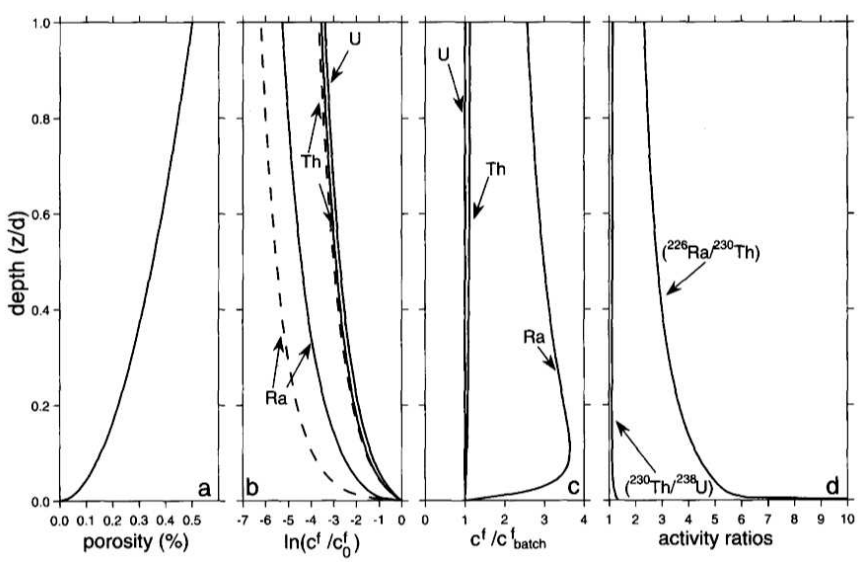

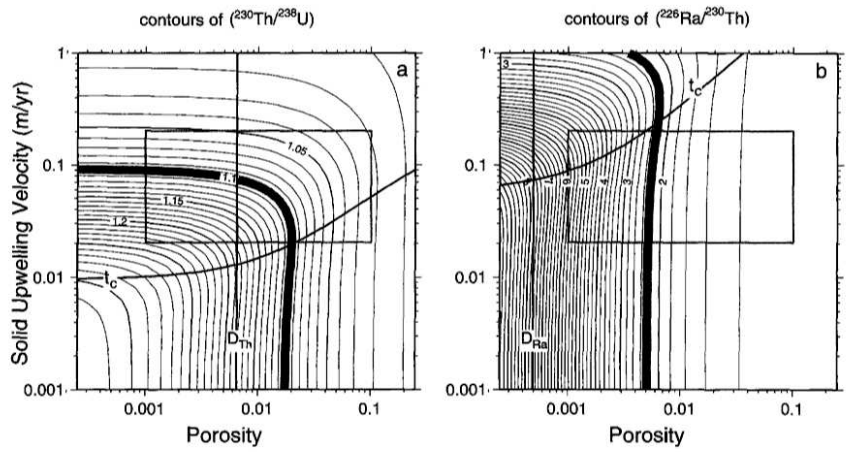

Fig. 5. Effect of upwelling rate W_0 and maximum porosity ϕ_{max} on activity ratios calculated for melt at the top of the upwelling column (contours). The maximum degree of melting for all calculations is $F = 0.25$, $d = 50$ km, and the partition coefficients are $D_U = 0.0086$, $D_{Th} = 0.0065$ and $D_{Ra} = 0.0005$. (a) Contours of activity ratios for (^{230}Th/^{238}U). (b) Contours of (^{226}Ra/^{230}Th). The thick shaded contours mark the reference activity ratios (^{230}Th/^{238}U) = 1.1 and (^{226}Ra/^{230}Th) = 2.25 shown in Fig. 1. Note that for both ^{230}Th and ^{226}Ra there are two different regimes, one where the activity ratio is sensitive to upwelling velocity, the other is where the activity is only sensitive to the porosity. The location of the two regimes is controlled by the half-life of each daughter nuclide and the ratio of their partition coefficients to the porosity. In each plot, the vertical line marks the solutions where the maximum porosity is equal to the partition coefficient. The bold curved line marks the extraction time $t_c = 6.64$. The grey boxes mark values of W_0 appropriate for moderate to fast spreading ridges and a range of plausible porosities. In this region, the thorium and radium contours are roughly orthogonal. Thus a small change in porosity can cause large changes in (^{226}Ra/^{230}Th) with negligible changes in (^{230}Th/^{238}U) which is consistent with observations (Fig. 1).

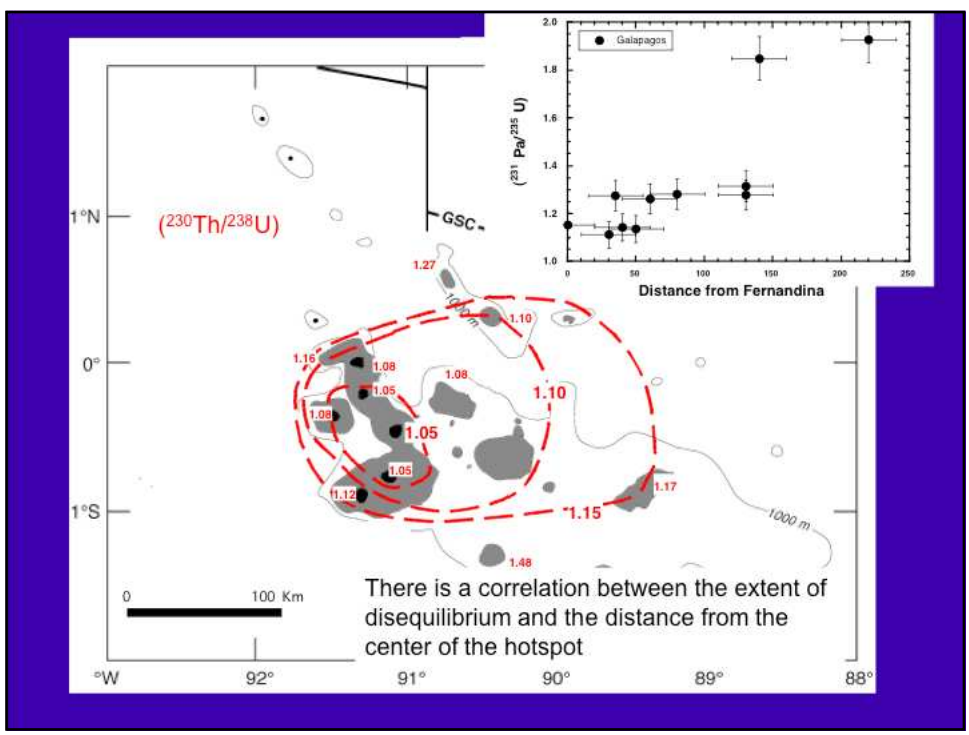

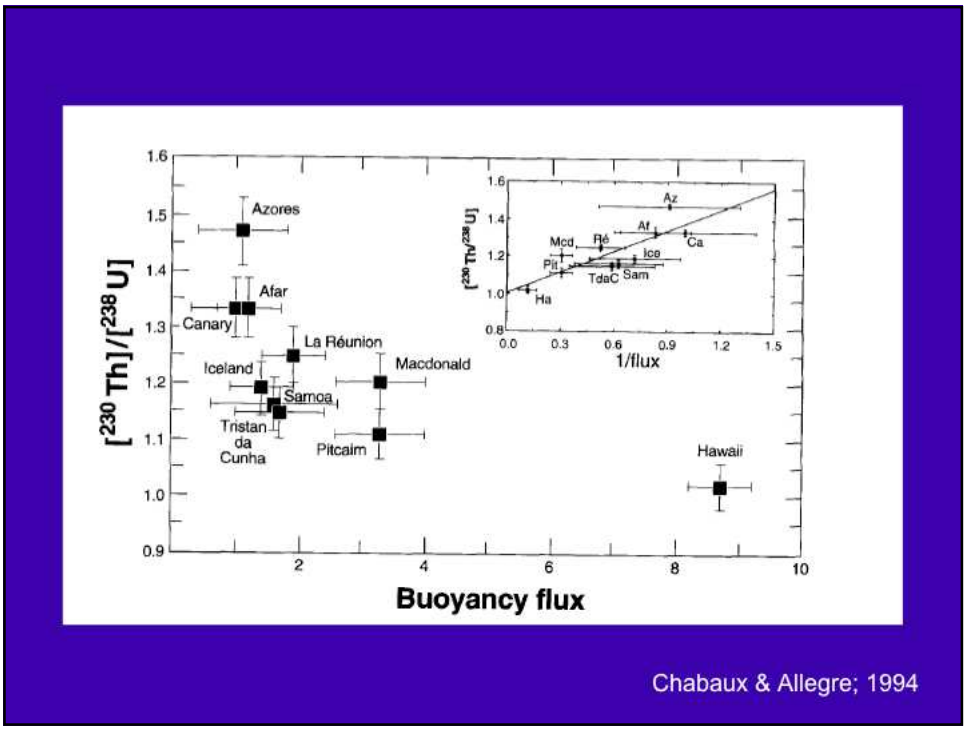

Chabaux & Allegre; 1994

Melts produced at higher-P are not in equilibrium with lherzolite or harzburgite at lower P (they are too SiO_2-poor). They react with the solid as they pass thru, precipitating OL and dissolving pyroxene.

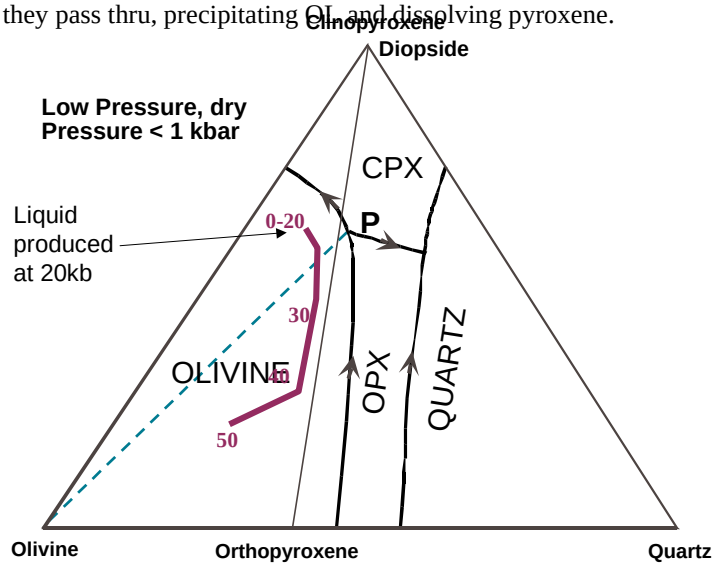

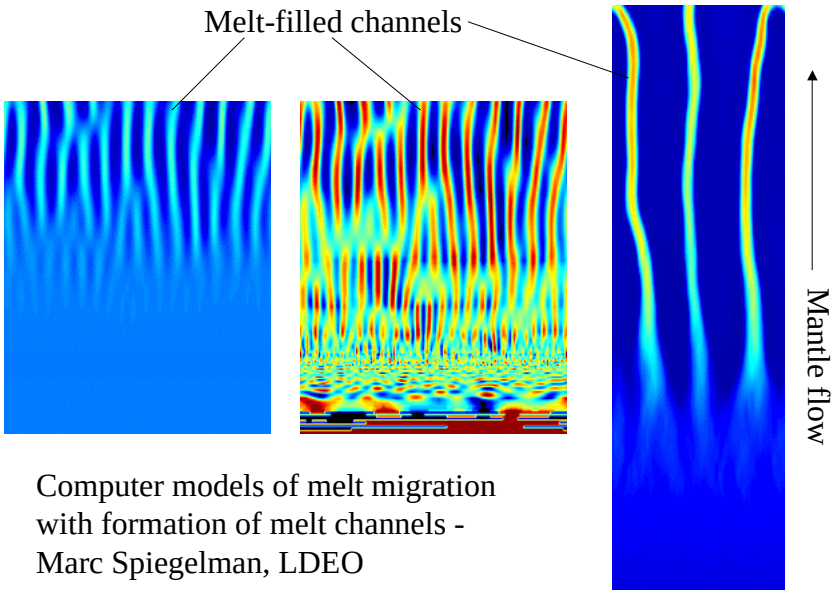

Computer models of melt migration with formation of melt channels - Marc Spiegelman, LDEO

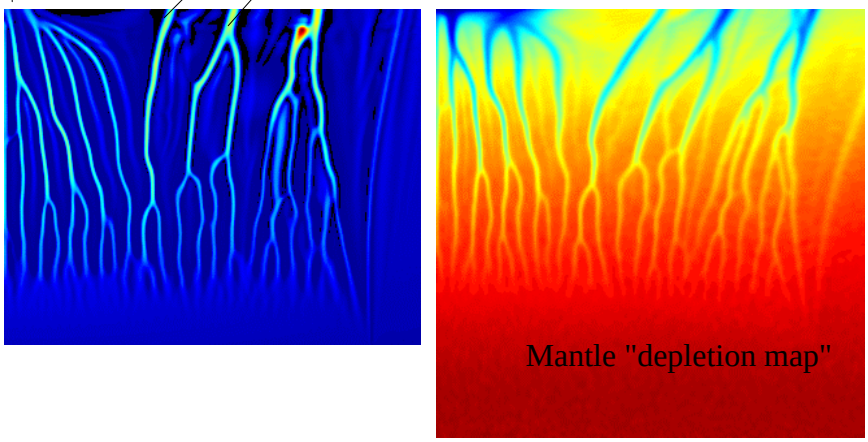

Mid Ocean Ridge computer models Marc Spiegelman, LDEO